J. Plasma Physics (2004), *vol.* 70, *part* 4, *pp.* 397–413.
DOI: 10.1017/S0022377803002575 Printed in the United Kingdom

Multi-dimensional transient process for a pulse ablating capillary discharge: modeling and experiment

BAOMING LI and DANIEL Y. KWOK†

Nanoscale Technology and Engineering Laboratory, Department of Mechanical Engineering, University of Alberta, Edmonton, AB, Canada T6G 2G8
(daniel.y.kwok@ualberta.ca)

(Received 17 January 2003)

Abstract. In recent years, ablative plasma generated by capillary discharge attracted considerable attention because of its possible applications in electrothermal launchers, laser-driven particle accelerators, thin-film deposition and soft X-ray lasers, etc. An electrical discharge through a capillary insulator heats the capillary plasma that provides further evaporation of the capillary wall and electrode. The created plasma is confined by the capillary wall, electrode material and flow in a specified chamber through a hollow electrode. The mass flux leaving the capillary in axial motion is replenished by a radial inward flow of matter. Thus the radial component of the mass flux plays a principal role in the mass and energy balance. In this paper, we present a theoretical model for a time-dependent magnetohydrodynamical simulation to calculate the dynamic evolution of plasma flow and transportation in two-dimensional configurations combined with turbulent effect. The thermodynamic and transport properties are characterized by a model that describes the plasma composition, equation of state, internal energy, viscosity and thermal and electrical conductivity for a partially ionized multi-component plasma in the weakly non-ideal region, similar to that which exists in the ablation-controlled arcs. Our model results show that some of the well-known experimental features of this kind of discharge are confirmed, particularly the radial mass and energy transportation.

1. Introduction

In recent years, ablative plasma occurring in electrical discharge inside capillaries has attracted great interest for a variety of applications, including optical guiding of high-power lasers [1,2], X-ray lasers [3,4], thin-film deposition [5], electrothermal-chemical launchers [6,7], plasma-propellant (or explosive) interactions [8,9], electric fuses and extreme-ultraviolet sources [10–14]. The first main application of ablative discharge is connected with the generation of high pressure in exploding fuses and in SF6 puffer self-pressure-generating circuit breakers [15–17]. In these devices, plasma discharge is initiated from a thin fuse wire and ablation of material by the discharge is sustained by the capillary surface. The ablated vapor increases

† Author to whom correspondence should be addressed.

the pressure within the capillary and plasma is expelled through an exit. Ablative discharge provides plasma with high density, temperature and flow velocity, leading to strong mass and energy fluxes.

For a better understanding of ablating capillary discharge, there is a need to control the plasma exit flux. Since the capillary made by commonly used polymers, such as polyethylene, is usually opaque, it is very difficult to investigate experimentally the evolution of the plasma inside the ablative capillaries. In fact, it has not yet been possible to obtain reliable experimental data concerning the temporal evolution and spatial dependence of the remaining plasma hydrodynamic and thermodynamic properties except for pressure inside the capillary. Thus, theoretical modeling of ablative discharge is required to evaluate the behavior of the plasma properties that are difficult to measure. It be should noted that measurements of the temporal evolution and spatial dependence of plasma hydrodynamic and thermodynamic properties can be found elsewhere [18]. However, the parameters related to flow field and ionization reaction inside the capillary are not available and are necessary to analyze the plasma transfer process and efficiency. Further, modeling of the ablative discharge is a complicated problem because it involves altogether Joule heating, radiative transport, dissipative phenomena and hydrodynamic flow. In the past, the problem has been solved with three forms of theoretical models. The first model assumed the case of a quasi-stationary one-dimensional system [19]; the second considered plasma flow in the axial direction as the main dynamic feature of the discharge based on more general quasi-one-dimensional time-dependent equations [20–22]; the third employed magneto-hydrodynamic equations with ablation as a source term to describe the capillary discharge [23].

In this paper, we present a theoretical model and simulation results from time-dependent magneto-hydrodynamical equations for dynamic evolution of plasma flow and transportation in two-dimensional configurations combined with turbulent effect. Our model is different from previous work in that the radiative transport of energy to the capillary wall can be treated reasonably by the boundary conditions at the capillary wall. In this work, the thermodynamic and transport properties of the plasma are characterized by a model that describes the plasma composition, equation of state, internal energy, viscosity and thermal and electrical conductivity for a partially ionized multi-component plasma in the weakly non-ideal region, similar to that exists in ablation-controlled arcs. We found that our model predictions are in good agreement with experimental results.

2. Model equations

2.1. Governing equations

We use here a two-dimensional axisymmetric set of hydrodynamic equations describing the conductive, radiative and ablative unsteady-state flow in a cylindrical capillary. The equation for the conservation of mass is

$$\frac{\partial \rho_i}{\partial t} + \nabla \cdot (\rho_i \vec{u}) = 0, \tag{1}$$

where subscript i represents the chemical species of type i in a plasma; typically, $i =$ C, H, O and N. The equation for the conservation of momentum is given by

$$\frac{\partial}{\partial t}(\rho \vec{u}) + \nabla \cdot (\rho u_j \vec{u}) = -\nabla P + \frac{\partial}{\partial x_j}\left[\mu\left(\frac{\partial u_i}{\partial x_j} + \frac{\partial u_j}{\partial x_i}\right)\right] \tag{2}$$

https://doi.org/10.1017/S0022377803002575 Published online by Cambridge University Press

and the equation for the conservation of energy is

$$\frac{\partial}{\partial t}(\rho E) + +\nabla \cdot (\rho \vec{u} E) + \nabla \cdot (P\vec{u}) = \frac{j^2}{\sigma} - \nabla \cdot q_r, \tag{3}$$

where j^2/σ is the Joule heating term; j is the plasma current density given by $j = I/\pi R^2$ with I being the electrical current flowing through the capillary; σ represents the electrical conductivity obtained from a computer program (see later); $\nabla \cdot q_r$ is the radiative conduction term; ρ, $\vec{u}$, P and E are the plasma density, flow velocity, pressure and total energy, respectively. The total energy E is the sum of kinetic and internal energies in a plasma. Under local thermodynamic equilibrium (LTE) conditions, the total energy E can be expressed as

$$\begin{aligned}\rho E = \frac{\rho|\vec{u}|^2}{2} + \Bigg\{ & \frac{3}{2} k_{\mathrm{B}} T \sum_j n_j (1 + \chi_{1j} + 2\chi_{2j}) + \sum_j [(I_{1j} - \Delta I_{1j}) n_j \chi_{1j} \\ & + (I_{1j} - \Delta I_{1j} + I_{2j} - \Delta I_{2j}) n_j \chi_{2j} + n_j (1 + \chi_{1j} + 2\chi_{2j}) W_{0j} \\ & + n_j \chi_{1j} W_{1j} + n_j \chi_{2j} W_{2j}] \Bigg\} + \rho(E_{\mathrm{V}} + E_{\mathrm{D}}),\end{aligned} \tag{4}$$

and the equation of state for the multi-component plasma becomes

$$P = \sum_j n_j (1 + \chi_{1j} + 2\chi_{2j}) k_{\mathrm{B}} T,$$

where n_j is the number density of the particles of type j in a plasma; χ_{ij}, I_{ij} and ΔI_{ij} are the number density, ionization energy and degeneration of ionization energy due to non-ideal plasma effect, respectively, for the ith ionized particles of type j in a plasma; E_{V} and E_{D} are the specific energy due to evaporation and dissociation, respectively. W_{ij} and u_{ij} are defined by the following expressions, respectively:

$$W_{ij} = -k_{\mathrm{B}} T^2 \frac{\partial}{\partial T} (\ln u_{ij}),$$

$$u_{ij} = \sum_k g_{ijk} \exp\left(-\frac{W_{ijk}}{k_{\mathrm{B}} T}\right),$$

where W_{ijk} and g_{ijk} are respectively the excitation energy and degeneracy in the kth state of the ith ionized particles of type j in a plasma. The heat flux due to radiation is

$$q''_{\mathrm{radiation}} = \rho_{\mathrm{D}} u \left(\frac{5}{2} R T_{\mathrm{D}} + \frac{u^2}{2} + \gamma\right), \tag{5}$$

where the subscript D represents the dissociation term, R is the gas constant and γ is the latent heat. Equation (5) was obtained by means of energy balance with the assumption that the total energy radiated by the plasma in the radial direction equates to that returned to the plasma by the ablated material. Equations (1)–(3) can be rewritten in dimensionless forms using the following normalization

$$\begin{aligned}\bar{r} = \frac{r}{r_0}, \quad \bar{z} = \frac{z}{r_0}, \quad \bar{u}_r = \frac{u_r}{u_0}, \quad \bar{u}_z = \frac{u_z}{u_0}, \quad \bar{t} = \frac{t}{t_0}, \\ \bar{\rho} = \frac{\rho}{\rho_0}, \quad \bar{P} = \frac{P}{P_0}, \quad \bar{T} = \frac{T}{T_0}, \quad \bar{E} = \frac{E}{u_0^2},\end{aligned} \tag{6}$$

https://doi.org/10.1017/S0022377803002575 Published online by Cambridge University Press

where r_0, P_0, T_0 and ρ_0 are the capillary radius, predefined maximum pressure, temperature and density, respectively; u_0 and t_0 are defined respectively as

$$u_0 = \sqrt{\frac{P_0}{\rho_0}}, \quad t_0 = \frac{r_0}{u_0}.$$

With the quantities defined in (6), (1)–(3) can be reduced to

$$\begin{aligned}
&\frac{\partial \bar{\rho}}{\partial \bar{t}} + \frac{\partial \bar{\rho}\bar{u}_r}{\partial \bar{r}} + \frac{\partial \bar{\rho}\bar{u}_z}{\partial \bar{z}} + \frac{\bar{\rho}\bar{u}_r}{\bar{r}} = 0,\\
&\frac{\partial \bar{\rho}\bar{u}_r}{\partial \bar{t}} + \frac{\partial}{\partial \bar{r}}\left[\bar{\rho}\bar{u}_r^2 + \bar{P} - \frac{2\mu}{u_0\rho_0 r_0}\frac{\partial \bar{u}_r}{\partial \bar{r}}\right] + \frac{\partial}{\partial \bar{z}}\left[\bar{\rho}\bar{u}_r\bar{u}_z - \frac{\mu}{u_0\rho_0 r_0}\left(\frac{\partial \bar{u}_r}{\partial \bar{z}} + \frac{\partial \bar{u}_z}{\partial \bar{r}}\right)\right]\\
&\quad + \frac{1}{\bar{r}}\left[\bar{\rho}\bar{u}_r^2 - \frac{2\mu}{u_0\rho_0 r_0}\frac{\partial \bar{u}_r}{\partial \bar{r}}\right] = 0,\\
&\frac{\partial \bar{\rho}\bar{u}_z}{\partial \bar{t}} + \frac{\partial}{\partial \bar{r}}\left[\bar{\rho}\bar{u}_r\bar{u}_z - \frac{\mu}{u_0\rho_0 r_0}\left(\frac{\partial \bar{u}_z}{\partial \bar{r}} + \frac{\partial \bar{u}_r}{\partial \bar{z}}\right)\right] + \frac{\partial}{\partial \bar{z}}\left[\bar{\rho}\bar{u}_z^2 + \bar{P} - \frac{2\mu}{u_0\rho_0 r_0}\frac{\partial \bar{u}_z}{\partial \bar{z}}\right] \quad (7)\\
&\quad + \frac{1}{\bar{r}}\left[\bar{\rho}\bar{u}_r\bar{u}_z - \frac{\mu}{u_0\rho_0 r_0}\left(\frac{\partial \bar{u}_z}{\partial \bar{r}} + \frac{\partial \bar{u}_r}{\partial \bar{z}}\right)\right] = 0,\\
&\frac{\partial \bar{\rho}\bar{E}}{\partial \bar{t}} + \frac{\partial}{\partial \bar{r}}\left[\bar{\rho}\bar{u}_r\bar{E} + \bar{P}\bar{u}_r + \frac{q_r}{\rho_0 u_0^3}\right] + \frac{\partial}{\partial \bar{z}}\left[\bar{\rho}\bar{u}_z\bar{E} + \bar{P}\bar{u}_z + \frac{q_z}{\rho_0 u_0^3}\right]\\
&\quad + \frac{1}{\bar{r}}\left[\bar{\rho}\bar{u}_r\bar{E} + \bar{P}\bar{u}_r + \frac{q_r}{\rho_0 u_0^3}\right] - \frac{j^2 r_0}{\sigma\rho_0 u_0^3} = 0.
\end{aligned}$$

2.2. Thermodynamic and transport properties of plasma mixtures

For ablation-controlled arcs occurring in electric discharge inside capillaries, a consequence of low temperature and highly charged particle density is that the Coulomb potential energy of plasma particles could possess the same order of magnitude as the kinetic energy. Thus, the ablation-controlled arc is a weakly ionized multi-component plasma mixture. Li et al. [24, 25] proposed a weak non-ideal plasma model to treat the thermodynamic and transport properties. The calculation procedures for a weak non-ideal plasma are as follows. (1) As a first step, the chemical composition of the plasma can be obtained by solving the mass action laws combined with the gas law and the condition of charge neutrality. (2) With the partition functions for the various species in the plasma, thermodynamic properties can be calculated in a straightforward manner using relations of statistical mechanics. The evaluation of non-ideal plasma electrical conductivity includes corrections to the Spitzer model as follows: (1) a modification of the shielding distance is implemented into the kinetic equations; (2) the interaction potential is modified to included short-distance collisions; (3) localization of low-energy electrons is considered; (4) Spitzer's expression corrected by consideration of electron–neutral collisions is added.

2.3. Boundary conditions

At the center line of the capillary, some of the terms in the governing equations will become infinite. Thus, we employ the limit theorem to obtain the governing

https://doi.org/10.1017/S0022377803002575 Published online by Cambridge University Press

Table 1. Boundary conditions of the ablative capillary discharge used in the two-dimensional axisymmetric modeling.

$r=0$ at the center line	$u_r=0$	$\dfrac{\partial u_z}{\partial r}=0$	$\dfrac{\partial P}{\partial r}=0$	$\dfrac{\partial T}{\partial r}=0$
$r=R$ at the surface	$u_r=0$	$u_z=0$	$\dfrac{\partial P}{\partial r}=0$	$-\left(\dfrac{k}{c_{\mathrm{P}}}\right)\dfrac{\partial h}{\partial r}=\dfrac{k_{\mathrm{c}}}{w}(T-T_{w,0})$
$z=0$ at the closed end	$u_r=0$	$u_z=0$	$\dfrac{\partial P}{\partial z}=0$	$\dfrac{\partial T}{\partial z}=0$
$z=1$ at the open end	$\dfrac{\partial u_r}{\partial z}=0$	$\dfrac{\partial u_z}{\partial z}=0$	$P=P_0$	$\dfrac{\partial T}{\partial z}=0$

equations at $\bar{r}=0$ as

$$\frac{\partial\bar{\rho}}{\partial\bar{t}}+\frac{\partial 2\bar{\rho}\bar{u}_r}{\partial\bar{r}}+\frac{\partial\bar{\rho}\bar{u}_z}{\partial\bar{z}}=0,$$

$$\frac{\partial\bar{\rho}\bar{u}_r}{\partial\bar{t}}+\frac{\partial}{\partial\bar{r}}\left[2\bar{\rho}\bar{u}_r^2+\bar{P}-\frac{4\mu}{\mu_0\rho_0 r_0}\frac{\partial\bar{u}_r}{\partial\bar{r}}\right]+\frac{\partial}{\partial\bar{z}}\left[\bar{\rho}\bar{u}_r\bar{u}_z-\frac{\mu}{u_0\rho_0 r_0}\left(\frac{\partial\bar{u}_r}{\partial\bar{z}}+\frac{\partial\bar{u}_z}{\partial\bar{r}}\right)\right]=0,$$

$$\frac{\partial\bar{\rho}\bar{u}_z}{\partial\bar{t}}+\frac{\partial}{\partial\bar{r}}\left[2\bar{\rho}\bar{u}_r\bar{u}_z-\frac{2\mu}{\mu_0\rho_0 r_0}\left(\frac{\partial\bar{u}_z}{\partial\bar{r}}+\frac{\partial\bar{u}_r}{\partial\bar{z}}\right)\right]+\frac{\partial}{\partial\bar{z}}\left[\bar{\rho}\bar{u}_z^2+\bar{P}-\frac{2\mu}{u_0\rho_0 r_0}\frac{\partial\bar{u}_z}{\partial\bar{z}}\right]=0,$$

$$\frac{\partial\bar{\rho}\bar{E}}{\partial\bar{t}}+\frac{\partial}{\partial\bar{r}}\left[2\bar{\rho}\bar{u}_r\bar{E}+2\bar{P}\bar{u}_r+\frac{2q_r}{\rho_0 u_0^3}\right]+\frac{\partial}{\partial\bar{z}}\left[\bar{\rho}\bar{u}_z\bar{E}+\bar{P}\bar{u}_z+\frac{q_z}{\rho_0 u_0^3}\right]-\frac{j^2 r_0}{\sigma\rho_0 u_0^3}=0. \quad (8)$$

On the surface of the capillary wall, we applied the heat flux equation to write the boundary condition at $\bar{r}=1$ as

$$-\left(\frac{k}{c_{\mathrm{P}}}\right)\frac{\partial h}{\partial r}=\frac{k_{\mathrm{c}}}{w}(T-T_{w,0}). \quad (9)$$

At the open end of the capillary, we used a third-order interpolation scheme in the immediate vicinity of the exit as

$$q(j,k)=q(j-3,k)+3[q(j-1,k)-q(j-2,k)]. \quad (10)$$

The boundary conditions used in our modeling are summarized in Table 1, where $T_{w,0}$, k_{c}, w, P_0 are the wall temperature, heat conductivity, wall thickness and pressure outside the capillary, respectively.

2.4. Numerical method

We solved the system of governing equations with the aid of an algorithm by a two-step explicit MacCormack scheme with an artificial viscosity. The two-dimensional compressible flow has the following general form

$$\bar{U}_t+F_r+G_z+H=0.$$

The explicit two-step algorithm with second-order accuracy in space can be

https://doi.org/10.1017/S0022377803002575 Published online by Cambridge University Press

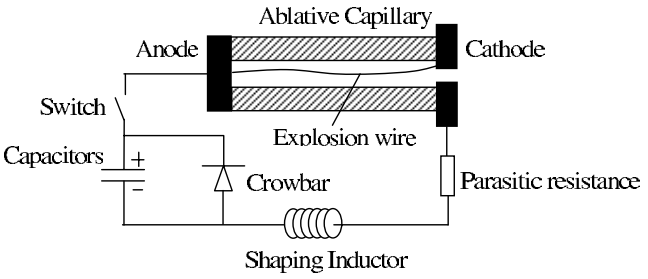

Figure 1. Schematic diagram of ablative capillary discharge.

expressed as

$$\begin{aligned}
\bar{U}_{j,k}^{\overline{n+1}} &= \bar{U}_{j,k}^{n} - \frac{\Delta t}{\Delta r}\left(F_{j+1,k}^{n} - F_{j,k}^{n}\right) - \frac{\Delta t}{\Delta z}\left(G_{j,k+1}^{n} - G_{j,k}^{n}\right) - \Delta t \cdot H_{j,k}^{n} \\
&\quad + \frac{Q_1}{2}\left(\bar{U}_{j+1,k}^{n} - 2\bar{U}_{j,k}^{n} + \bar{U}_{j-1,k}^{n}\right) + \frac{Q_2}{2}\left(\bar{U}_{j,k+1}^{n} - 2\bar{U}_{j,k}^{n} + \bar{U}_{j,k-1}^{n}\right), \\
\bar{U}_{j,k}^{n+1} &= \frac{1}{2}\left(\bar{U}_{j,k}^{n} + \bar{U}_{j,k}^{\overline{n+1}}\right) - \frac{\Delta t}{2\Delta r}\left(F_{j,k}^{\overline{n+1}} - F_{j-1,k}^{\overline{n+1}}\right) - \frac{\Delta t}{2\Delta z}\left(G_{j,k}^{\overline{n+1}} - G_{j-1,k}^{\overline{n+1}}\right) \\
&\quad - \frac{\Delta t}{2} \cdot H_{j,k}^{\overline{n+1}} + \frac{Q_1}{2}\left(\bar{U}_{j+1,k}^{n+1} - 2\bar{U}_{j,k}^{n+1} + \bar{U}_{j-1,k}^{n+1}\right) \\
&\quad + \frac{Q_2}{2}\left(\bar{U}_{j,k+1}^{n+1} - 2\bar{U}_{j,k}^{n+1} + \bar{U}_{j,k-1}^{n+1}\right),
\end{aligned} \tag{11}$$

where

$$Q_1 = \frac{\left|P_{j+1,k}^{n} - 2P_{j,k}^{n} + P_{j-1,k}^{n}\right|}{\left|P_{j+1,k}^{n} + 2P_{j,k}^{n} + P_{j-1,k}^{n}\right|},$$

$$Q_2 = \frac{\left|P_{j,k+1}^{n} - 2P_{j,k}^{n} + P_{j,k+1}^{n}\right|}{\left|P_{j,k+1}^{n} + 2P_{j,k}^{n} + P_{j,k+1}^{n}\right|}.$$

3. Results and discussion

3.1. Comparison with experimental data

A schematic diagram of the capillary discharge device is shown in Fig. 1. The experimental setup used to study the ablative discharge of the capillary consists of a high-density polyethylene capillary, a copper–tungsten rear electrode and a steel nozzle. The capillary was contained within a glass fiber filament-wound body. Electric current can be supplied from a pulsed power supply via an axial copper rod to the rear electrode whose tip protruded into the rear of the capillary. A length of tinned copper wire was soldered to the rear electrode tip, passing along the length of the capillary and fixing to the front section of the nozzle (by passing the wire through a small hole). The pulsed power supply used was a single-module capacitor bank (1200 μF) charged to 3 kV and fitted with a 25-μH pulse-shaping inductor. The stored energy on the capacitor was approximately 5.4 kJ. Measurements of the electrical parameters of the plasma were made using a Rogowski coil and a 2000:1 voltage divider. The experimental parameters used to validate the model prediction are 1200 μF for capacitance, 3 kV for charged voltage, 25 μH for inductance, 36 mm for capillary length and 3 mm for capillary diameter. Details of the experimental setup can be found elsewhere [26].

https://doi.org/10.1017/S0022377803002575 Published online by Cambridge University Press

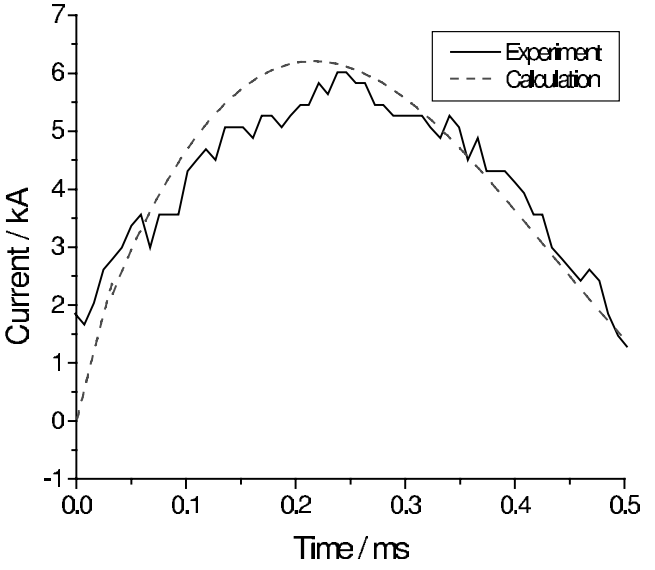

Figure 2. Comparison of discharge current flowing in the plasma between model prediction and experiment.

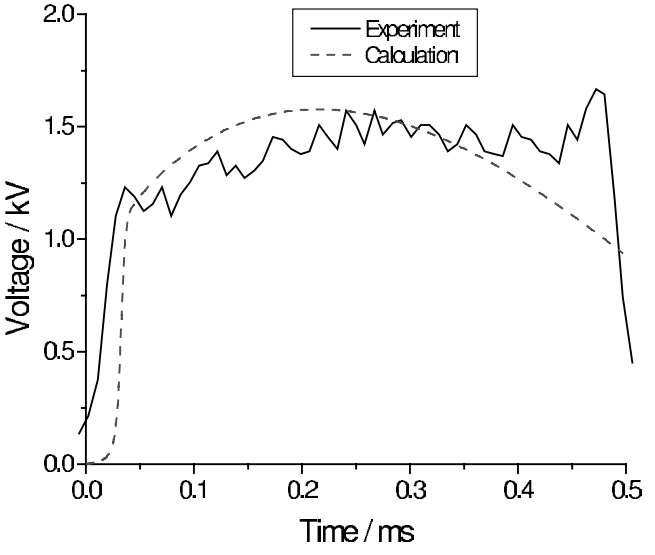

Figure 3. Comparison of voltage across the capillary between model prediction and experiment.

For ablative capillary discharge, the only reliable measurements of the discharge parameters have been the electrical characteristics such as the current and voltage between capillary electrodes. Thus, we employed the measured current and voltage versus time curves to validate the prediction of our two-dimensional axisymmetric model. We show in Figs 2 and 3 the comparison between our model prediction and experimental results [26] for the discharge current through and voltage across the capillary, respectively. Since we employed a tinned copper wire to initiate the

https://doi.org/10.1017/S0022377803002575 Published online by Cambridge University Press

Table 2. Comparison of mean resistance during the main discharge between the experiments and predictions corresponding to the experimental conditions in Table 3.

Number	1	2	3	4	5	6
Experiments (mΩ)	82.7	46.4	79.4	89.6	217.8	259.1
Predictions (mΩ)	82.7	46.4	78.8	91.1	216.2	258.0

Table 3. Experimental conditions for the ablating polyethylene-capillary discharges.

Number	Capacitance (μF)	Charged voltage (kV)	Shaping inductance (μH)	Capillary length (mm)	Capillary diameter (mm)
1	1200	12	25	80	5
2	1200	10	25	20	5
3	1200	10	25	36	3
4	1200	8	25	80	5
5	1200	5	25	80	5
6	1200	3	25	36	3

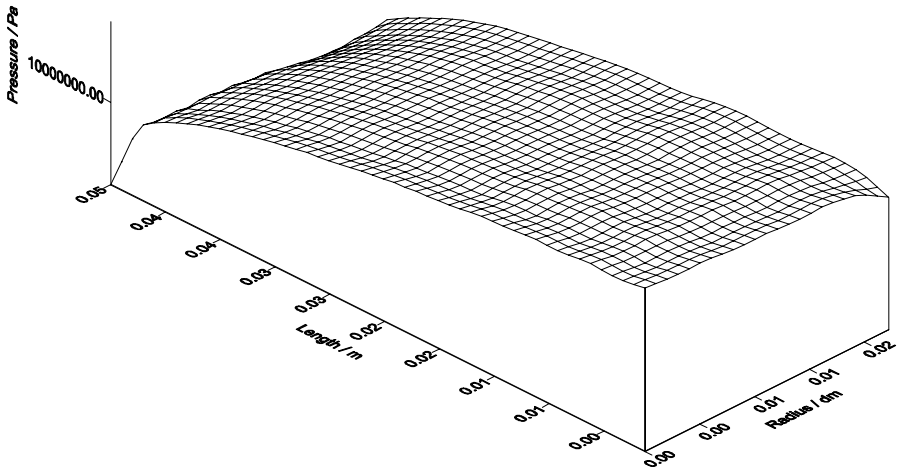

Figure 4. Spatial profile of plasma pressure at the instant 200 μs with laminar model.

ablating capillary discharge, the electrical exploding process of copper wire can lead to a large electromagnetic interference (EMI) with the Rogowsky coil. As a fibre-optical link was used for data transmission, the initial data signal from the Rogowsky coil may be distorted by the EMI. Therefore, it is difficult to obtain zero current I and voltage V pulses experimentally at $t = 0$ in Figs 2 and 3. Nevertheless, the good agreement in Figs 2 and 3 indicates that our description regarding the thermodynamic and transport properties of weak non-ideal plasma for ablative discharge is adequate. This can also be reflected by comparing the experimental results of plasma resistivity (determined from $I(t)$ and $V(t)$) with those predicted. The results are given in Table 2 for six individual experiments with the details in Table 3; Table 2 suggests that an agreement of better than 5% for the plasma

https://doi.org/10.1017/S0022377803002575 Published online by Cambridge University Press

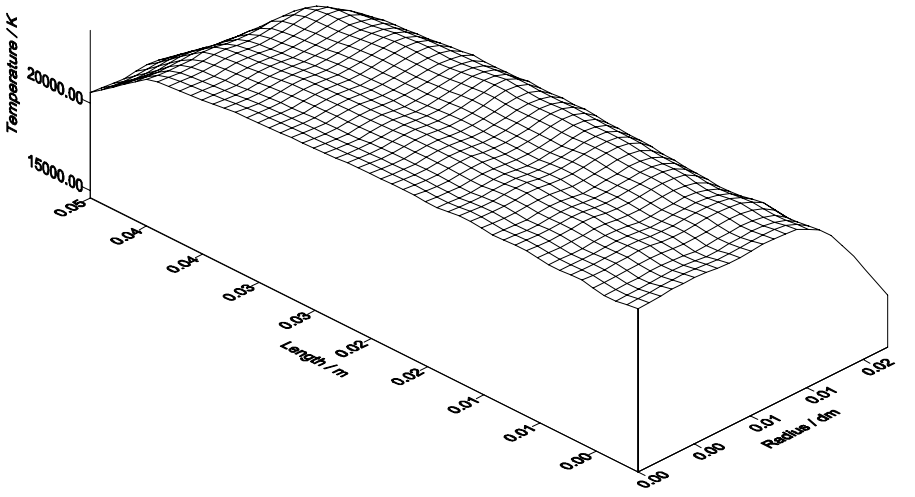

Figure 5. Spatial profile of plasma temperature at the instant 200 μs with laminar model.

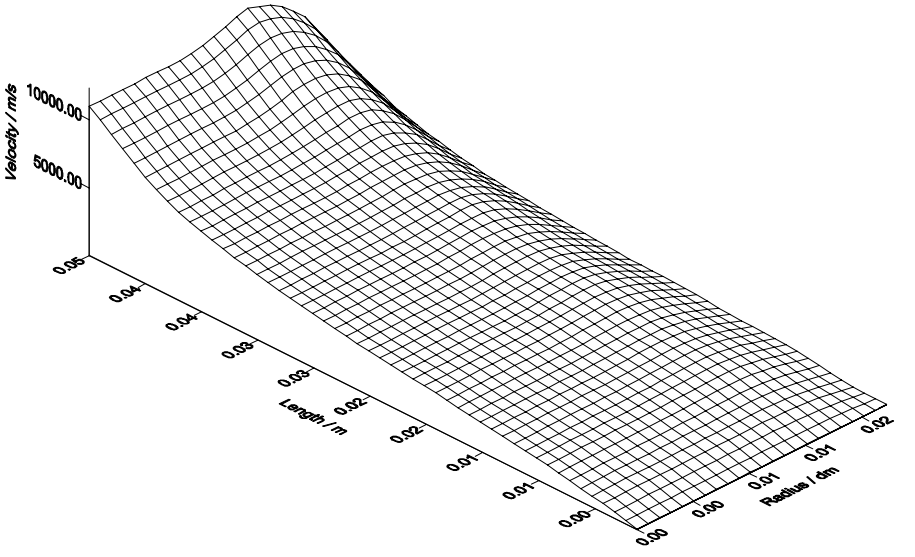

Figure 6. Spatial profile of plasma velocity at the instant 200 μs with laminar model.

resistivity can be obtained. This, however, does not guarantee the same accuracy for the predictions of the density and temperature profiles inside the capillary.

3.2. Numerical results of plasma laminar flow

Using the physical model presented here (given by the set of equations (7)), we simulate the temporal and spatial behavior of other plasma properties by the assumption of laminar flow. We consider a hypothetical capillary made from polyethylene having 50 mm in length and 2.5 mm in radius. The stored energy on the capacitor was approximately 40 kJ. As a high-energy system, it is charged to 8 kV with a 25-μH pulse-shaping inductor. The calculated spatial profiles of the

https://doi.org/10.1017/S0022377803002575 Published online by Cambridge University Press

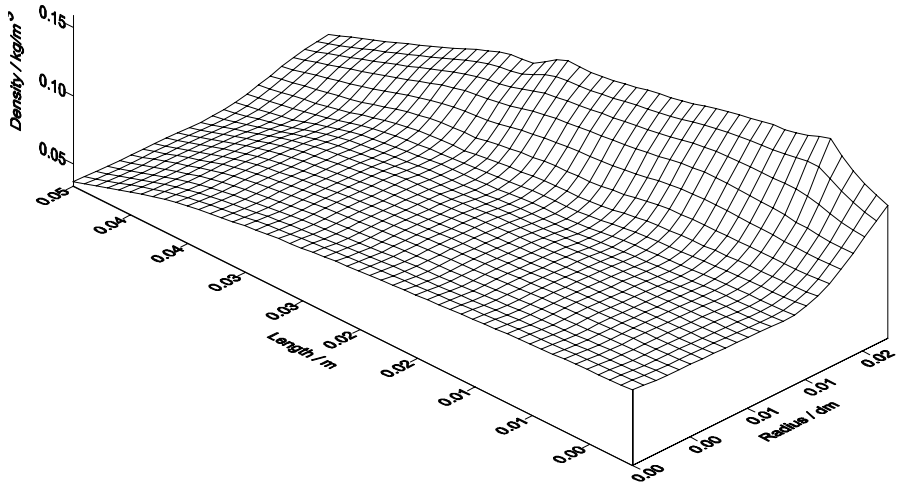

Figure 7. Spatial profile of plasma density at the instant 200 μs with laminar model.

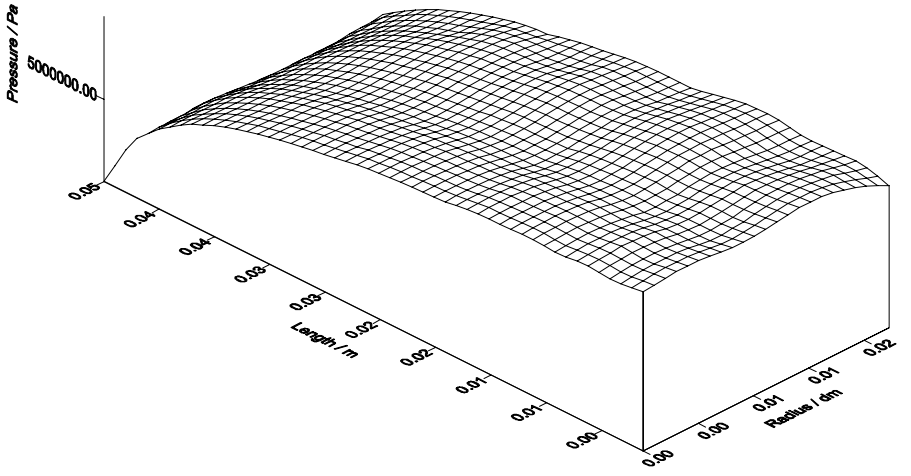

Figure 8. Spatial profile of plasma pressure at the instant 200 μs with turbulent model.

plasma properties for pressure, temperature, velocity and density are shown in Figs 4–7, respectively, at the instant of 200 μs. We see that our two-dimensional simulation could reflect the spatial variation of plasma characteristics. Figures 4–7 illustrate a strong increase in velocity, and large pressure, temperature, velocity and mass-density gradients at the capillary exit. This behavior represents a typical critical flow of high-energy ablative discharge [27,28]. We found that the maximum values of pressure, temperature and density can be reached at the closed end of the capillary during the entire duration of the discharge. The sharp decrease in temperature and increase in mass density in the immediate vicinity of the capillary wall surface can be explained by wall ablation of the capillary. This strong decrease in velocity in the immediate vicinity of the wall surface of the capillary is due to viscosity interaction. From the results in these figures, we conclude that plasma flow in the axial direction is the main dynamical feature of the discharge. Further,

https://doi.org/10.1017/S0022377803002575 Published online by Cambridge University Press

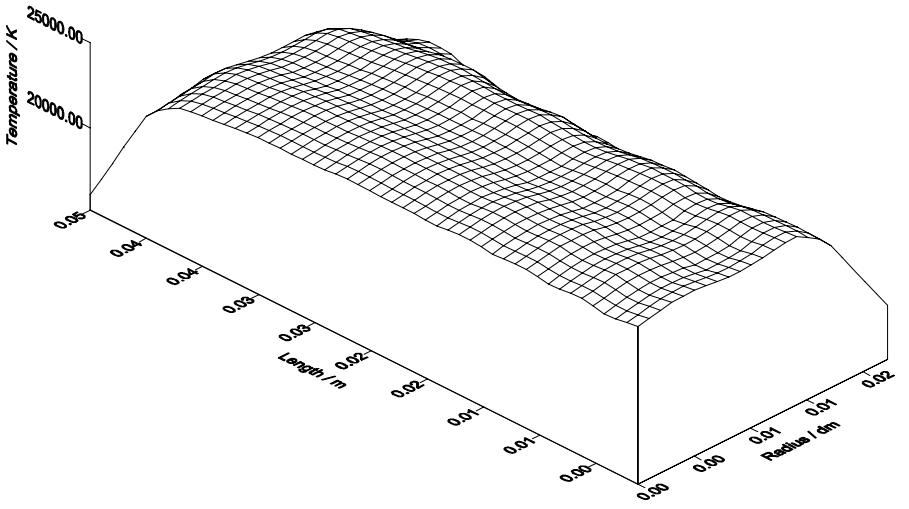

Figure 9. Spatial profile of plasma temperature at the instant 200 μs with turbulent model.

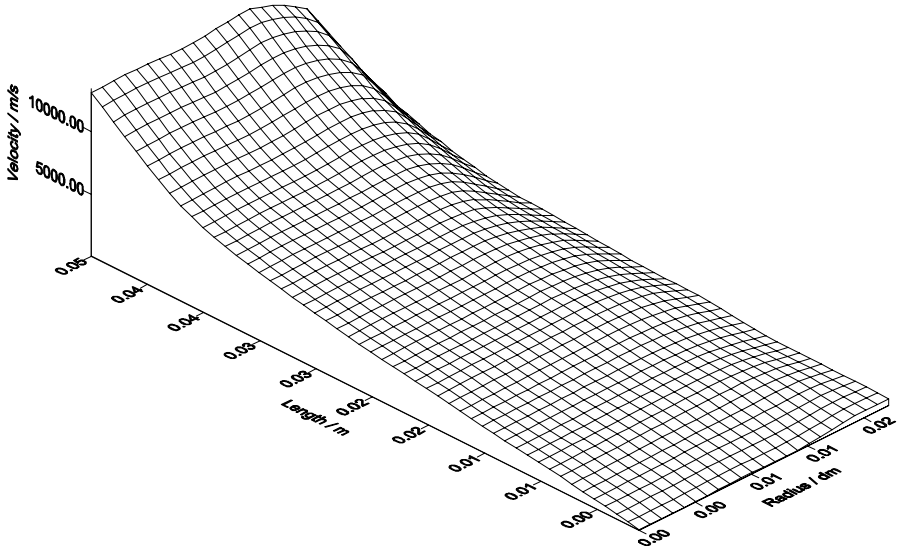

Figure 10. Spatial profile of plasma velocity at the instant 200 μs with turbulent model.

the ablative capillary discharge develops a steady-state-like behavior for a long period. The plasma characteristics in the immediate vicinity of the wall surface of the capillary have a strong variation due to the interaction between the plasma and the capillary wall.

3.3. Numerical results of plasma turbulent flow

In the ablative discharge capillary, the Reynolds number can be as high as 10^5. In this flow regime, the plasma should be turbulent. Normally, the capillary has a large length to diameter ratio. Thus, in order to investigate the effects of turbulence on the plasma characteristics, it is reasonable to employ a mixing length model for

https://doi.org/10.1017/S0022377803002575 Published online by Cambridge University Press

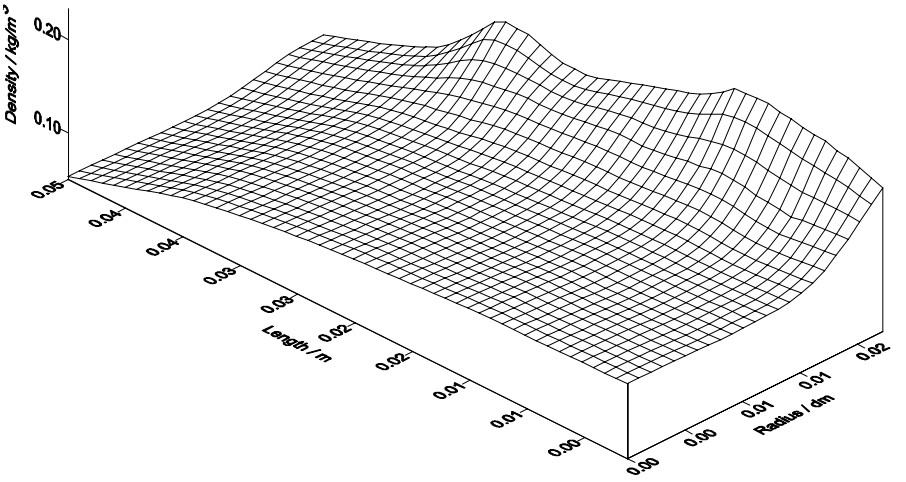

Figure 11. Spatial profile of plasma density at the instant 200 μs with turbulent model.

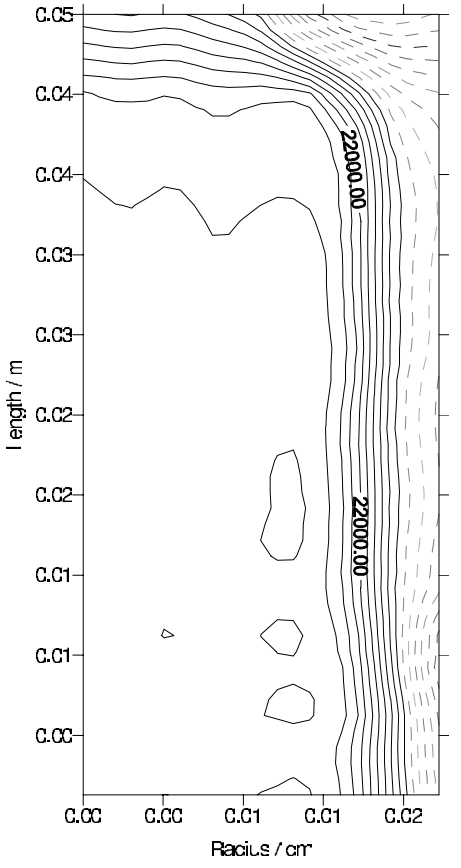

Figure 12. Plasma-temperature contour with laminar model at the instant 200 μs.

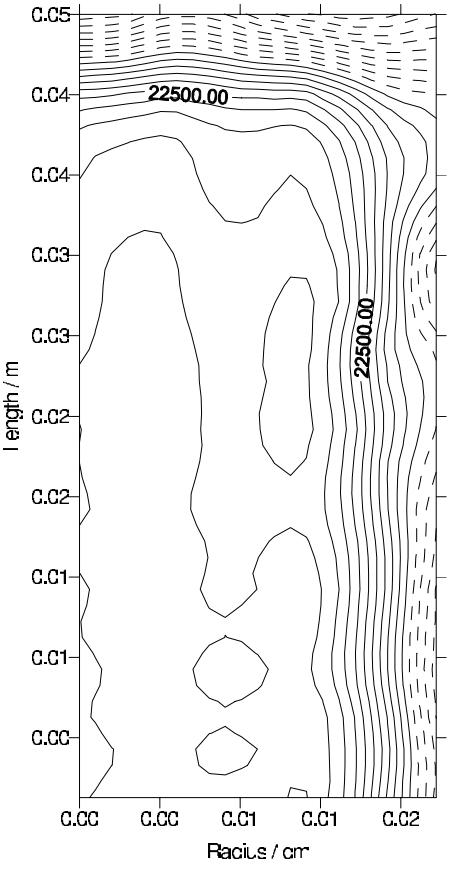

Figure 13. Plasma-temperature contour with turbulent model at the instant 200 μs.

https://doi.org/10.1017/S0022377803002575 Published online by Cambridge University Press

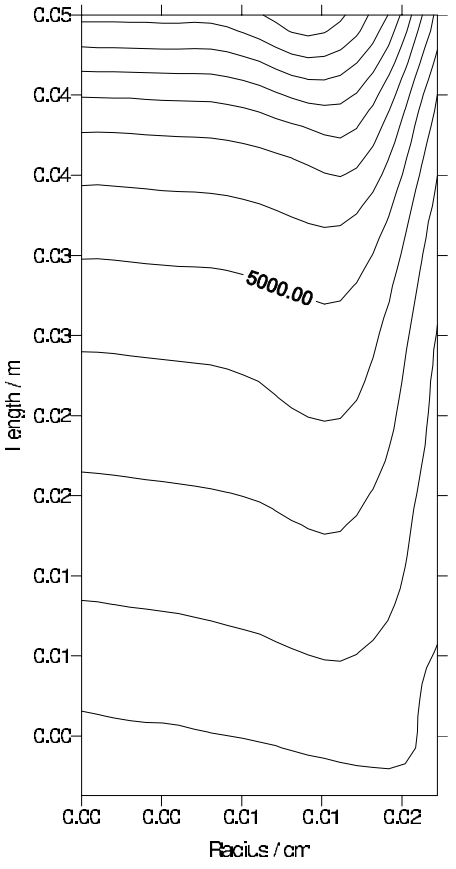

Figure 14. Plasma-velocity contour with laminar model at the instant 200 μs.

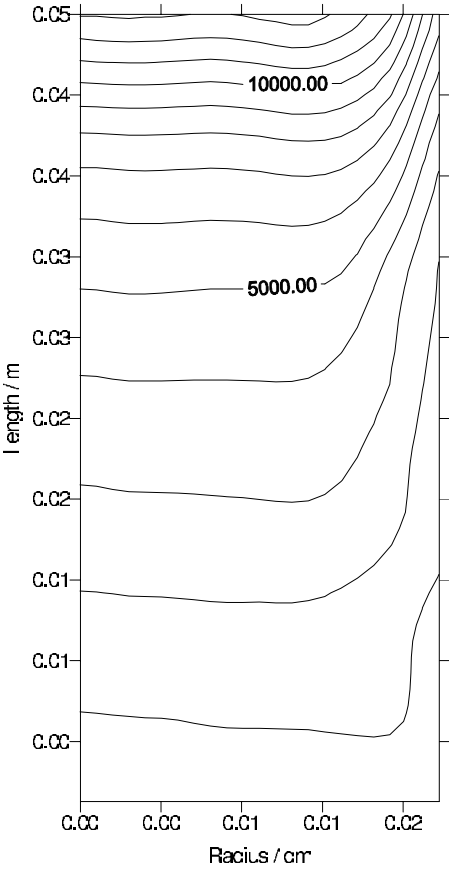

Figure 15. Plasma-velocity contour with turbulent model at the instant 200 μs.

turbulent flow. The governing equations in this particular case can be written as

$$
\begin{aligned}
&\frac{\partial \rho}{\partial t}+\frac{\partial \rho u_r}{\partial r}+\frac{\partial \rho u_z}{\partial z}+\frac{\rho u_r}{r}=0,\\
&\frac{\partial \rho u_r}{\partial t}+\frac{\partial}{\partial r}\left[\rho u_r^2+P-2(\mu+\mu_t)\frac{\partial u_r}{\partial r}\right]\\
&\quad+\frac{\partial}{\partial z}\left[\rho u_r u_z-(\mu+\mu_t)\left(\frac{\partial u_r}{\partial z}+\frac{\partial u_z}{\partial r}\right)\right]=0,\\
&\frac{\partial \rho u_z}{\partial t}+\frac{\partial}{\partial r}\left[\rho u_r u_z-(\mu+\mu_t)\left(\frac{\partial u_z}{\partial r}+\frac{\partial u_r}{\partial z}\right)\right]\\
&\quad+\frac{\partial}{\partial z}\left[\rho u_z^2+P-2(\mu+\mu_t)\frac{\partial u_z}{\partial z}\right]=0,\\
&\frac{\partial \rho E}{\partial t}+\frac{\partial}{\partial r}[\rho u_r E+P u_r+q_r]+\frac{\partial}{\partial z}[\rho u_z E+P u_z+q_z]\\
&\quad+\frac{1}{r}[\rho u_r E+P u_r+q_r]-\frac{j^2}{\sigma}=0,
\end{aligned}
\tag{12}
$$

https://doi.org/10.1017/S0022377803002575 Published online by Cambridge University Press

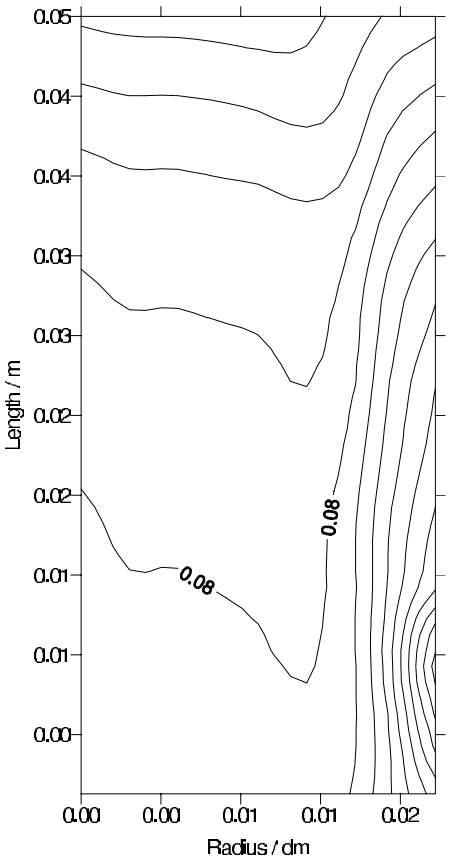

Figure 16. Plasma-density contour with laminar model at the instant 200 μs.

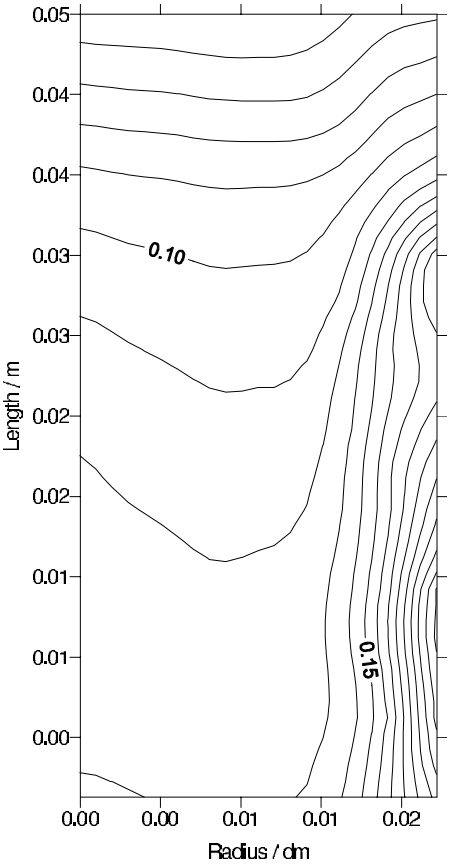

Figure 17. Plasma-density contour with turbulent model at the instant 200 μs.

where $\mu_t = \rho l_m^2 |du/dr|$; u is a time-averaged velocity for potential flow; and l_m is the mixing length. Here, we employed the Nikurades relation for a circular pipe to calculate the mixing length [29]:

$$\frac{l_m}{r_0} = 0.14 - 0.08\left(1 - \frac{r}{R}\right)^2 - 0.06\left(1 - \frac{r}{R}\right)^4 \quad \text{for Re} = 1.1 \times 10^5 – 3.2 \times 10^6. \quad (13)$$

Figures 8–11 show the spatial dependence of the main plasma properties, respectively, for pressure, temperature, velocity and density using a turbulent model. We see that both the turbulent and laminar models considered here could reflect the basic plasma characteristics of ablative capillary discharge. However, there are some apparent difference between the results obtained from the two numerical models. The fluctuation of the various results in the vicinity of the capillary wall from the turbulent model can be explained by the viscosity dissipation due to boundary effects by the turbulent motion. We should point out that the influence of viscosity dissipation outside the boundary layer becomes negligible. We also see from the temperature distribution in Fig. 8 that the boundary turbulent interaction can indeed enhance the ablation rate and produce a more irregular shape. We conclude that the spatial dependence of the ablation rate along the capillary follows closely

https://doi.org/10.1017/S0022377803002575 Published online by Cambridge University Press

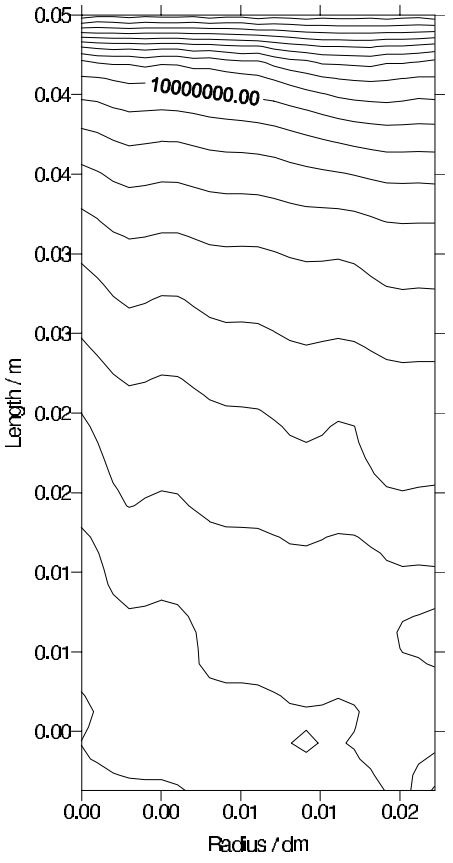

Figure 18. Plasma-pressure contour with laminar model at the instant 200 μs.

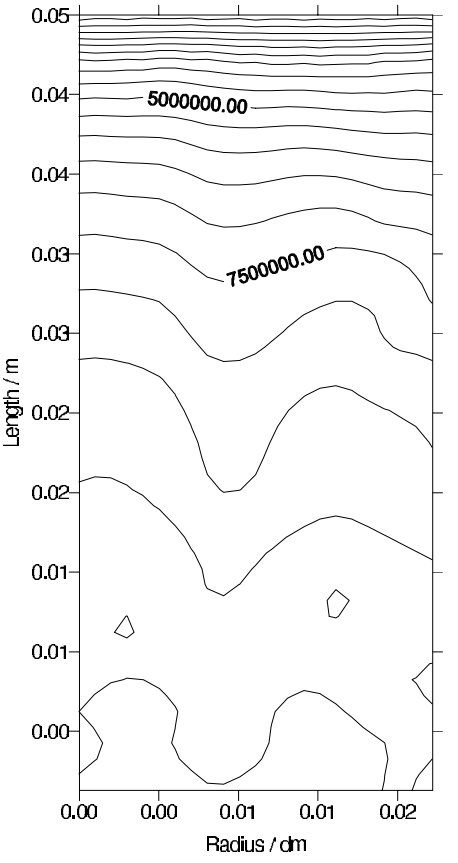

Figure 19. Plasma-pressure contour with turbulent model at the instant 200 μs.

the temperature changes due to strong boundary interaction. Further, we also conclude that major changes of the parameters occur near the immediate vicinity of the capillary wall and exit.

Figures 12–20 reflect the flow field of ablative discharge plasma at the instant of 200 μs, corresponding to the maximum input power from the laminar and turbulent flow, respectively. As shown in these figures, the height coordinate is the capillary length; the width coordinate is the capillary radius. Among the results obtained, we found that the temperature contour of the laminar flow model shows smoother results than those of the turbulent flow model. From the temperature contour of laminar flow model, it is obvious to observe the boundary layer in the form of a regular shape. The irregularity in the temperature contour and relatively narrow boundary layer were caused by strong turbulent interaction in the immediate vicinity of the capillary wall. It is important to note that the plasma with temperature over 20 000 K dominates in most of the space inside the capillary. As is well known, it is crucial to produce a high-energy ablative discharge for a variety of applications as previously mentioned. From the mass-density contour of the plasma, the ablation rate is dependent on the temperature change in the immediate vicinity of the capillary wall.

https://doi.org/10.1017/S0022377803002575 Published online by Cambridge University Press

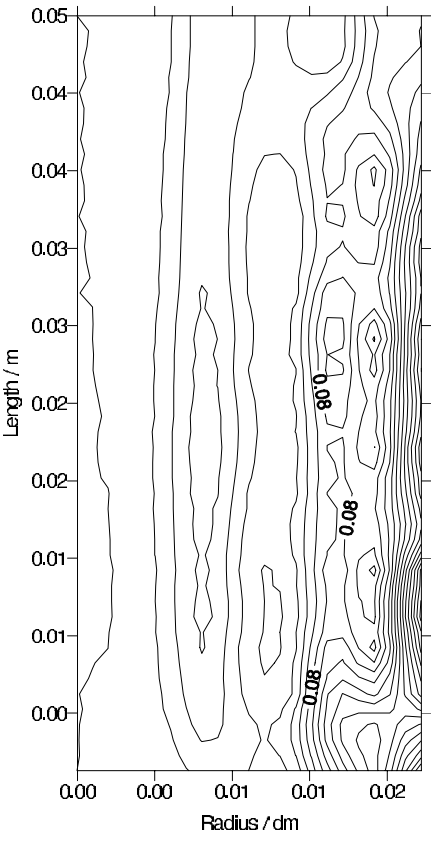

Figure 20. Plasma-vortex viscosity contour with turbulent model at the instant 200 μs.

It is interesting to note that the velocity distribution along the radial direction from the turbulent model is smoother than that of the laminar one. Since the statistical state of fluctuation that the length scale of turbulent motion should be small enough with sufficiently high Reynolds number, it can be treated as smooth and isotropic. That is to say, practically, the small scale of uniformity shown in the turbulent model is reasonable. Figure 20 shows the contour of vortex viscosity. It reflects a high turbulent mixing in the immediate vicinity of the capillary wall. Finally, the predictions obtained from the theoretical model with turbulent flow appear to be more acceptable.

4. Summary

We have compared theoretical simulation and experimental results for an ablative discharge using the assumptions of laminar and turbulent flow. Excellent agreement was found between model prediction and experimental results for both laminar and turbulent approximations. We found irregularity in the temperature contour due to strong flow interaction with the immediate vicinity of the capillary wall. We conclude that the small scale of uniformity in the turbulent results suggest that the use of the turbulent model appears to be more acceptable.

https://doi.org/10.1017/S0022377803002575 Published online by Cambridge University Press

Acknowledgements

We gratefully acknowledge financial support from the Alberta Ingenuity Establishment and Student Funds, Canada Research Chair (CRC) Program, Canada Foundation for Innovation (CFI), Petro-Canada Young Innovator Fund, and Natural Science and Engineering Research Council of Canada (NSERC) in support of this research.

References

[1] Zigler, A., Ehrlich, Y., Cohen, C., Krall, J. and Sprangle, P. 1996 *J. Opt. Soc. Am.* B **13**, 68.
[2] Ehrlich, Y., Zigler, A., Cohen, C., Krall, J. and Sprangle, P. 1996 *Phys. Rev. Lett.* **77**, 4186.
[3] Lee, R. W. and Zigler, A. 1988 *Appl. Phys. Lett.* **53**, 2028.
[4] Rocca, J. J., Shlyaptsev, V. and Tomasel, F. G. 1994 *Phys. Rev. Lett.* **73**, 2192.
[5] Rocca, J. J., Cortazar, O. D., Tomasel, F. G. and Szapiro, B. T. 1993 *Phys. Rev.* E **48** 2378.
[6] Zhou, X., Li, Y., Wang, J. and Huang, Z. 2001 *IEEE Trans. Plasma Sci.* **29**, 360.
[7] Hankins, O. E., Bourham, M., Earnhart, J. and Gilligan, J. 1993 *IEEE Trans. Magn.* **29**, 1158.
[8] Hankins, O. E., Bourham, M. and Mann, D. 1997 *IEEE Trans. Magn.* **33**, 259.
[9] Kim, J. U., Kim, K. J., Wilson, D. E., Peterson, D. R. and Clemens, N. T. 2000 *IEEE Trans. Plasma Sci.* **28**, 312.
[10] Muller, L. 1993 *J. Phys. D: Appl. Phys.* **26**, 1253.
[11] Domejean, E., Chevrier, P. F. C. and Petit, P. 1997 *J. Phys. D: Appl. Phys.* **30**, 2132.
[12] Kukhlevsky, S. V., Kaiser, J., Samek, O., Liska, M. and Erostyak, J. 2000 *J. Phys. D: Appl. Phys.* **33**, 1090.
[13] Burton, R. L. and Turchi, P. J. 1998 *J. Propulsion Power* **14**, 716.
[14] Hong, D., Dussart, R., Cachoncinlle, C., Rosenfeld, W., Gotze, S., Pons, J., Viladrosa, R., Fleurier, C. and Pouvesle, J. M. 2000 *Rev. Sci. Instrum.* **71**, 15.
[15] Chan, S. K., Fang, M. T. C. and Cowley, M. D. 1978 *IEEE Trans. Plasma Sci.* **6**, 399.
[16] Fang, M. T. C. and Newland, D. B. 1983 *J. Phys. D: Appl. Phys.* **16**, 793.
[17] Fang, M. T. C. and Guo, Z. Y. 1993 Proc. ICPIG XXI **2**, 48.
[18] Tomasel, F. G., Rocca, J. J., Cortazar, O. D. and Szapiro, B. T. 1993 *Phys. Rev.* E **47**, 2590.
[19] Loeb, A. and Kaplan, Z. 1989 *IEEE Trans. Magn.* **25**, 342.
[20] Zoler, D. and Cuperman, S. 1993 *J. Plasma Sci.* **50**, 51.
[21] Gilligan, J. G. and Mohanti, R. B. 1990 *IEEE Trans. Plasma Sci.* **18**, 190.
[22] Kennaugh, R. J. and Woods, L. C. 1995 *IEEE Trans. Magn.* **31**, 431.
[23] Hewkin, D. and Figura, E. 1993 *IEEE Trans. Magn.* **29**, 561.
[24] Li, B., Li, H. and Shen, Z. 1999 *Chinese J. Ballistics* **11**, 16.
[25] Li, B. and Li, H. 1999 In: *Proc. 12th IEEE Int. Pulsed Power Conf.* Lawrence Livermore National Laboratory, CA.
[26] Li, B., Li, H. and Yuan, W. 2000 *Exp. Meas. Fluid Mech. Chin.* **14**, 12.
[27] Zoler, D. and Alimi, R. 1995 *J. Phys. D: Appl. Phys.* **28**, 1141.
[28] Zoler, D., Saphier, D. and Alimi, R. 1994 *J. Phys. D: Appl. Phys.* **27**, 1423.
[29] Schlichting, H. 1968 *Boundary-layer Theory*. London: Pergamon Press.